Materials and Design 86 (2015) 305–312

Contents lists available at ScienceDirect

Materials and Design

journal homepage: www.elsevier.com/locate/jmad

Experimental study of the crystal structure of the $Mg_{15-x}Zn_xSr_3$ ternary solid solution in the Mg–Zn–Sr system at 300 °C

Jian Wang [a,*], Yi-Nan Zhang [b], Pierre Hudon [c], In-Ho Jung [c], Patrice Chartrand [a], Mamoun Medraj [b,d]

[a] Center for Research in Computational Thermochemistry (CRCT), Dept. of Chemical Engineering, École Polytechnique, Montréal, Québec H3C 3A7, Canada
[b] Department of Mechanical Engineering, Concordia University, 1455 De Maisonneuve Blvd. West, Montreal, Quebec H3G 1M8, Canada
[c] Department of Mining and Materials Engineering, McGill University, 3610 University Street, Montreal, Quebec H3A 0C5, Canada
[d] Department of Mechanical and Materials Engineering, Masdar Institute, Masdar City P.O. Box 54224, Abu Dhabi, United Arab Emirates

ARTICLE INFO

Article history:
Received 8 April 2015
Received in revised form 4 July 2015
Accepted 6 July 2015
Available online 15 July 2015

Keywords:
Ternary compound
Mg alloys
Phase diagram
Crystal structure
X-ray
SEM/EDS
EPMA

ABSTRACT

A new ternary compound, $Mg_{15-x}Zn_xSr_3$ with extensive solid solubility in the Mg–Zn–Sr system was observed and studied using electron probe microanalysis (EPMA), scanning electron microscopy SEM, and X-ray techniques. The solid solubility limits of this compound were found to be $Mg_{15-x}Zn_xSr_3$ ($0.24 \le x \le 10.58$, at.%) at 300 °C using a diffusion couple and several equilibrated alloys. Analysis of the X-ray diffraction (XRD) patterns was carried out by Rietveld method. XRD data has shown that this solid solution crystallizes in the hexagonal $P6_3/mmc$ (194) space group with the $Ni_{11}Si_4Sc_3$ prototype. The lattice parameters decrease linearly with decreasing Mg content indicating substitutional solid solubility. The fractional atomic occupancy of the 6h, 6g, 4f, 2b and 12k sites of this compound are function of Mg content.

1. Introduction

Magnesium-based alloys are widely used in the automotive and aeronautic industries because magnesium is the lightest structural material with a density of about 1.80 g/cm^3. This interest in magnesium alloys arises from their low density, potentially high strength/weight ratios, good processing properties, and near complete recycling potential [1–4]. Actually, their high strength-to-weight ratio makes them even more attractive than steels [5] and plastics in many applications. The Mg–Zn series is the first hardenable Mg-based alloys developed for structural materials [6–9]. The solid solubility of Zn in the Mg (hcp) phase and the considerable amount of secondary precipitates in the Mg matrix can produce a very good age-hardening effect [10]. Unfortunately, the Mg–Zn series has the same problem as the Mg–Al series (but not the AE series), that is, poor mechanical properties at elevated temperatures which restrict their applications [2]. Recently, strontium has drawn much attention [11–14] as an important additive in Mg-based alloys for improving relatively high temperature mechanical properties. According to Baril et al. [14], the micro-alloying of strontium in magnesium alloys (e.g., Mg–Zn, Mg–Al based alloys) permits to obtain superior creep performance and excellent high-temperature properties. Moreover, Hirai et al. [15] reported that by adding Sr, high strength and improved creep resistance could be obtained for cast AZ91 magnesium alloy. For Nakaura et al. [16], Sr additions can also help to reduce the hot-cracking effect of Ca containing Mg–Al based alloys. Recently, Mg–Zn–Sr alloys were found to have a low degradation rate and moderate mechanical properties, which makes them potential biodegradable alloy candidates [17,18].

In the ternary Mg–Zn–Sr system, the phase diagrams of the three bounding binaries (Mg–Zn [19], Mg–Sr [20] and Zn–Sr [21]) have been satisfactorily investigated; the final accepted versions of each binary phase diagram are shown in Fig. 1. The phase diagram of the Mg–Zn binary system shows 5 intermetallic compounds, Mg_2Zn_{11}, $MgZn_2$, Mg_2Zn_3, $Mg_{12}Zn_{13}$, and $Mg_{51}Zn_{20}$, and two terminal solid solutions, hcp (Mg) and hcp (Zn). It is worth noting that the $Mg_{51}Zn_{20}$ compound is only stable between 325 and 342 °C. The phase diagram of the Mg–Sr binary system consists of 7 phases: hcp (Mg), fcc (Sr), bcc (Sr), $Mg_{17}Sr_2$, $Mg_{38}Sr_9$, $Mg_{23}Sr_6$, and Mg_2Sr. For the Zn–Sr binary system, 4 stoichiometric compounds are known to exist, ZnSr, Zn_2Sr, Zn_5Sr, and $Zn_{13}Sr$, plus three terminal solid solutions with limited solid solubility. Aljarrah et al. [22] extrapolated the Mg–Zn–Sr ternary system within the CALPHAD method [23] based on the binary thermodynamic parameters without considering the presence of ternary compounds and solid solubility of each binary compound. Experimental data on the Mg–Zn–Sr ternary system could not be found in the literature.

* Corresponding author at: Center for Research in Computational Thermochemistry (CRCT), Canada.
E-mail address: jian.wang@polymtl.ca (J. Wang).

http://dx.doi.org/10.1016/j.matdes.2015.07.038
0264-1275/

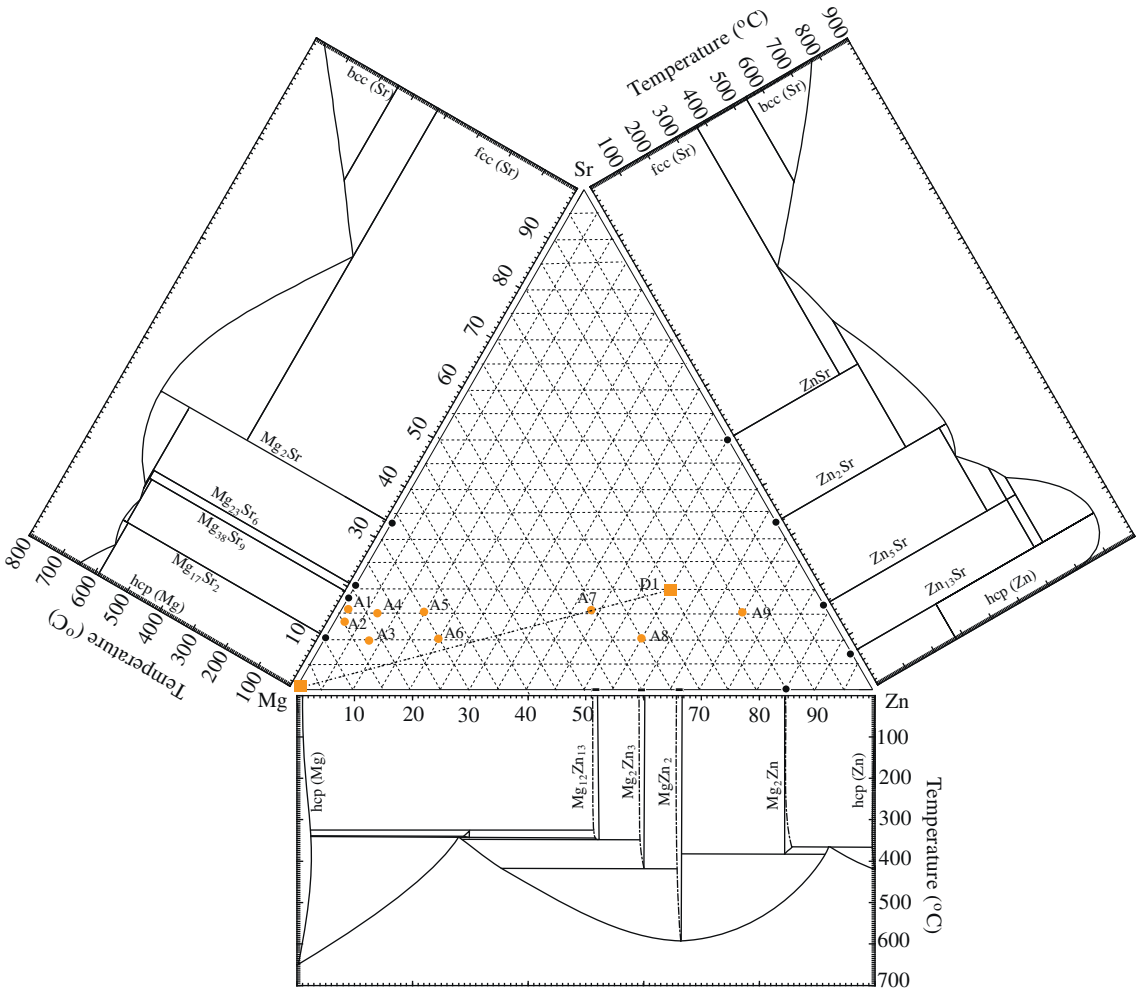

Fig. 1. The reported experimental binary phase diagrams [12–14] of the Mg–Zn–Sr system along with the nominal compositions of key samples prepared in the present work.

Since Sr is promising as an important alloying element for Mg-based alloys (such as the Mg–Zn and Mg–Al series), a thorough understanding of the phase equilibria in the Mg–Zn–Sr ternary system is much needed. In this paper, the isothermal section at 300 °C is studied by a diffusion couple and several equilibrated key samples, as described in the following section. To this end, the solid solubility and crystal structure of the new $Mg_{15-x}Zn_xSr_3$ ternary solid solubility limits at 300 °C is studied in the present work for the first time using EDS, EPMA, X-ray, and Rietveld techniques, which is a part of a wider thermodynamic database development project for the Mg–Zn–X (X: Ag, Ca, In, Li, Na, Sr, and Zn) multi-component systems [24–28].

2. Experimental procedures

The solid solubility limits of the $Mg_{15-x}Zn_xSr_3$ phase were determined using a diffusion couple with Mg–$Mg_{25}Zn_{55}Sr_{20}$ (at.%) alloy as end-members and with 9 key samples; it is should be noted that all the compositions of samples and their constituted phases were designated

Table 1
Compositions of equilibrium phases in the Mg–Zn–Sr ternary system as determined in the present work.

Sample no.	Alloy nominal composition (at.%)	Phase equilibria	Measured equilibrium phase compositions determined by EPMA (at.%)								
		Phase 1/Phase 2/Phase 3	Phase 1 ($Mg_{11}Zn_4Sr_3$)			Phase 2			Phase 3		
			Mg	Zn	Sr	Mg	Zn	Sr	Mg	Zn	Sr
A1	$Mg_{83}Zn_1Sr_{16}$	$Mg_{15-x}Zn_xSr_3/Mg_{17}Sr_2/Mg_{38}Sr_9$	81.6	1.3	17.1	88.1	0.6	11.3	79.4	0.6	20.0
A2	$Mg_{85}Zn_3Sr_{12}$	$Mg_{15-x}Zn_xSr_3/Mg_{17}Sr_2$	81.4	3.2	15.4	88.4	1.3	10.3	–	–	–
A3	$Mg_{83}Zn_7Sr_{10}$	$Mg_{15-x}Zn_xSr_3/Mg_{17}Sr_2$	77.0	7.5	15.5	86.1	3.7	10.2	–	–	–
A4	$Mg_{78}Zn_7Sr_{15}$	$Mg_{15-x}Zn_xSr_3/Mg_{17}Sr_2$	73.2	11.9	14.9	83.6	6.4	10.0	–	–	–
A5	$Mg_{70}Zn_{25}Sr_{15}$	$Mg_{15-x}Zn_xSr_3/Mg_{23}Sr_6$	69.0	14.7	16.3	69.0	10.5	20.5	–	–	–
A6	$Mg_{70}Zn_{20}Sr_{10}$	$Mg_{15-x}Zn_xSr_3/Mg_{17}Sr_2$	60.0	24.8	15.2	73.2	17.1	9.7	–	–	–
A7	$Mg_{40}Zn_{44}Sr_{16}$	$Mg_{15-x}Zn_xSr_3/Mg_2Sr/IM2$[a]	39.6	44.3	16.1	66.7	1.2	32.1	43.9	23.5	32.6
A8	$Mg_{35}Zn_{55}Sr_{10}$	$Mg_{15-x}Zn_xSr_3/IM3$[a]	33.8	49.5	16.7	36.3	54.8	8.9	–	–	–
A9	$Mg_{20}Zn_{65}Sr_{15}$	$Mg_{15-x}Zn_xSr_3/IM4$[a]/IM5[a]	24.9	58.8	16.3	11.8	79.6	8.6	20.4	61.8	17.8

[a] Note: IM2 to IM5 are new found phases which have been analyzed, and the identification results will be published in an upcoming paper.

in the present work using atomic percentage at.%. their nominal compositions are shown in Fig. 1 and given in Table 1. The diffusion end-members and key alloys were prepared from pure Mg (99.8 wt.%), Zn (99.5 wt.%), and Sr (99 wt.%) and melted in a frequency induction furnace under high purity argon atmosphere. The Sr pieces were kept in oil after weighing due to their high reactivity with oxygen. Before melting, each Sr piece was washed with 99 wt.% ethanol to remove the oil. In order to minimize the interaction of the samples with the crucibles, cubic-shaped crucibles were made using Ta foil (99.5 wt.% purity, 0.15 mm thickness). All the samples were melted in the induction furnace under

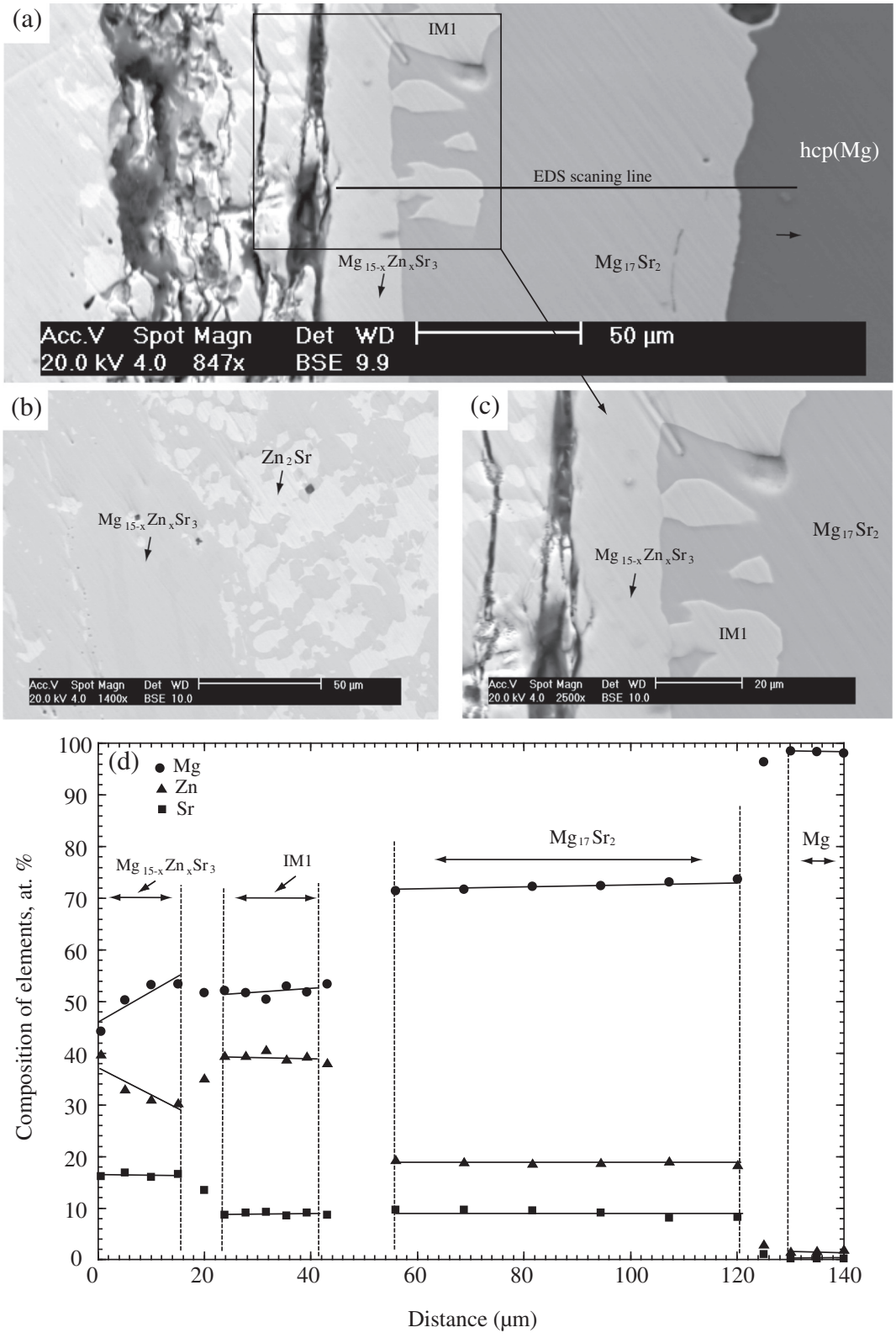

Fig. 2. Backscattered electron image of the diffusion couple annealed at 300 °C for 3 weeks: a) overall diffusion microstructure of diffusion couple, (b) microstructure of end-member $Mg_{25}Zn_{55}Sr_{20}$, (c) magnification of the selected diffusion layers, and (d) compositions of the elements in the constituted phases analyzed by EDS.

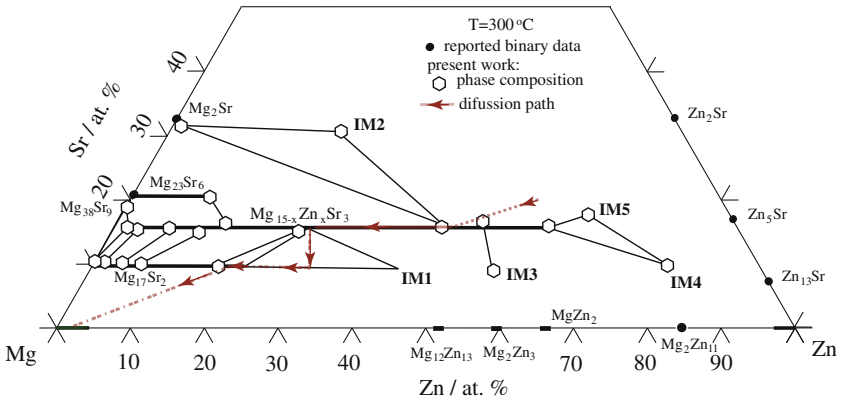

Fig. 3. Diffusion paths, solid solubility and partial phase equilibrium relationships of $Mg_{15-x}Zn_xSr_3$ compound as determined in the present work (thin black lines present the tie(s) line between/among the equilibrated phases, and thick black lines present each single phase with extend solid solubility).

argon atmosphere using this crucible. All samples were re-melted at least 3 times in order to obtain a homogenous microstructure. The Mg–Zn–Sr diffusion couple and all key samples were then sealed into quartz capsules under argon atmosphere and equilibrated at 300 °C for 21 and 35 days, respectively. Quenching was carried out in water without breaking the quartz tubes to prevent the oxidation of sample with water.

EPMA of the annealed samples was performed with JEOL 8900 probe using wavelength-dispersive spectroscopy (WDS). An accelerating voltage of 15 kV was used with a 20 nA beam current, a spot size of 2 μm and counting times of 20 s on peaks and 10 s on backgrounds. Raw data were reduced with the Phi-rho-Z (PRZ) correction using pure Mg, Zn metal and SrO standards. Phase relationships and constitutions of diffusion couples were determined using SEM equipped with energy-dispersive spectroscope (EDS).

Crystal structures of the phases present in the annealed samples were identified by X-ray analysis. XRD patterns were obtained with the PANanalytical X'pert Pro powder X-ray diffractometer using CuKα radiation at 45 kV and 40 mA. The XRD patterns were acquired from 20 to 120° (2θ) with a 0.02° step size. Then the collected patterns were analyzed with the X'Pert HighScore plus Rietveld analysis software in combination with the Pearson's crystal database [29]. The Si was used as an internal calibration standard enabled correcting the zero shift and specimen surface displacement which are the most serious systematic errors in X-ray powder diffraction patterns.

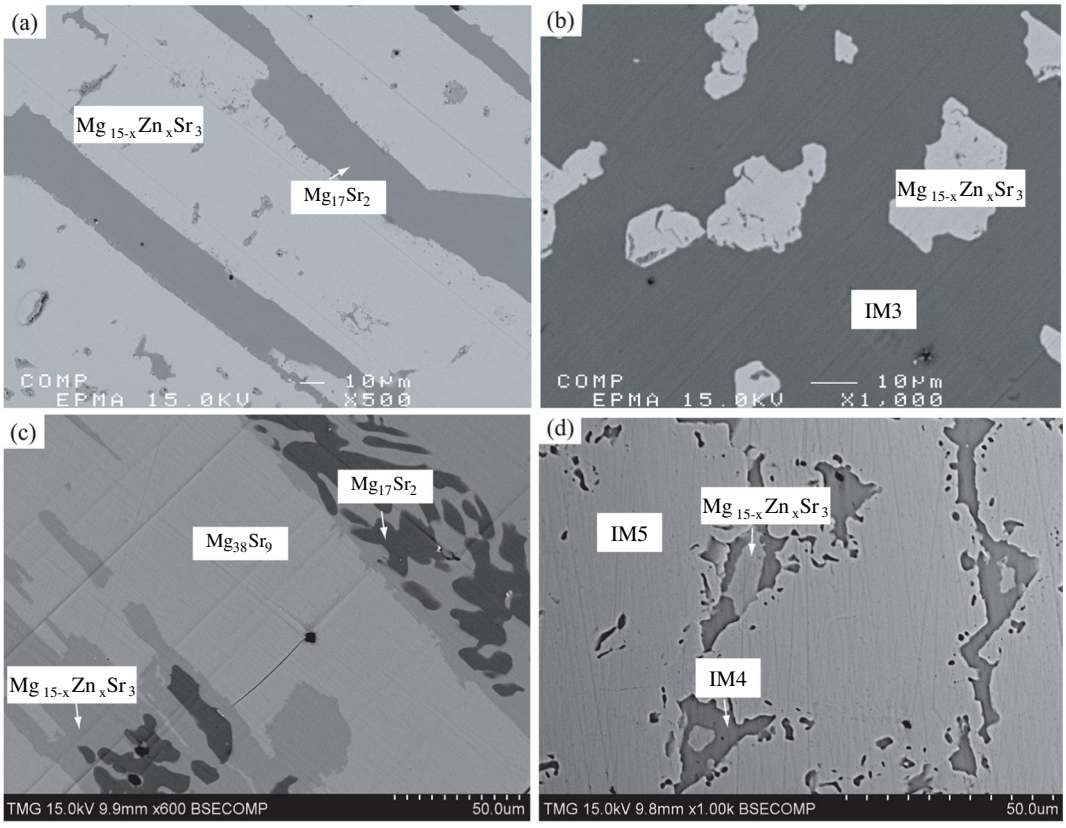

Fig. 4. Back-scattered (BSE) electron images of the typical ternary Mg–Zn–Sr alloys: (a) A4 ($Mg_{78}Zn_7Sr_{15}$), (b) A8 ($Mg_{35}Zn_{55}Sr_{10}$), (c) A1 ($Mg_{83}Zn_1Sr_{16}$), and (d) A9 ($Mg_{20}Zn_{65}Sr_{15}$) annealed at 300 °C for 35 days.

3. Results and discussions

3.1. Solid solution analysis

In order to obtain some knowledge of the equilibrium phase relationships in the Mg–Zn rich side (Sr ≤ 33 at.%) of the Mg–Zn–Sr ternary system at 300 °C, a solid–solid diffusion couple (designated D1) was prepared with end-members of Mg–$Mg_{25}Zn_{55}Sr_{20}$ as can be seen in Fig. 1. Backscattered electron images of this diffusion couple annealed at 300 °C for 3 weeks are depicted in Fig. 2. As shown in Fig. 2a, several diffusion layers can be clearly observed. Unfortunately, the diffusion layer(s) at the $Mg_{25}Zn_{55}Sr_{20}$ side was/were lost due to cracks that could not be avoided. However, the two-phase equilibria $Mg_{15-x}Zn_xSr_3$ + Zn_2Sr can be observed in the end-member $Mg_{25}Zn_{55}Sr_{20}$ (Fig. 2b). The magnification of the selected diffusion layers is shown in Fig. 2c. As can be seen in Fig. 2c, another new phase designated as IM1, which is equilibrated with $Mg_{15-x}Zn_xSr_3$ and $Mg_{17}Sr_2$, could also be observed in this diffusion couple. Compositions of the elements in the constituted phases were analyzed by EDS as shown in Fig. 2d. According to the acquired line scan results, the $Mg_{15-x}Zn_xSr_3$ compound form a substitutional solid solution from 29 to 37 at.% Zn at a constant Sr content of about 16.7 at.%.

As illustrated in Figs. 2 and 3, the diffusion path, Zn_2Sr + $Mg_{15-x}ZnxSr_3$↔ $Mg_{15-x}Zn_xSr_3$ ↔ $Mg_{17}Sr_2$ + IM1 ↔ $Mg_{17}Sr_2$ ↔ $Mg_{17}Sr_2$ + hcp (Mg) ↔ hcp (Mg), was identified in the diffusion couple D1.

Based on the phase equilibria relationships obtained from this diffusion couple, nine additional alloys (A1–A9) were prepared to determine the solid solubility limits and crystal structure of the new found compound $Mg_{15-x}Zn_xSr_3$ at 300 °C.

A few backscattered electron (BSE) images of such typical ternary Mg–Zn–Sr alloys are shown in Fig. 4. The microstructures of the two phase equilibria $Mg_{15-x}Zn_xSr_3$ + $Mg_{17}Sr_2$ in samples A4 ($Mg_{78}Zn_7Sr_{15}$) was observed as shown in Fig. 4(a). The two phase equilibrated microstructure of $Mg_{15-x}Zn_xSr_3$ + IM3 in sample A8 ($Mg_{35}Zn_{55}Sr_{10}$) as show in Fig. 4(b). The gray phase (labeled IM3) shown in Fig. 4(b) is another new ternary compound which will be discussed in a future paper. The minimum solid solubility limit of Zn was obtained to be 1.3 at.% from the sample A1 ($Mg_{83}Zn_1Sr_{16}$), where a three-phase equilibrium $Mg_{15-x}Zn_xSr_3$ + $Mg_{17}Sr_2$ + $Mg_{38}Sr_9$ was observed as shown in Fig. 4(c). The maximum solid solubility limit of Zn in $Mg_{15-x}Zn_xSr_3$ was obtained to be 58.8 at.% from the sample A9 ($Mg_{20}Zn_{65}Sr_{15}$), where a three-phase equilibrium $Mg_{15-x}Zn_xSr_3$ + IM4 + IM5 was observed as shown in Fig. 4(d). Moreover, the phases, light gray (named IM4) and deep dark (named IM5), are also new phases in this system which will be discussed in details in a future paper.

Furthermore, the constituted phases in all equilibrated samples were identified by XRD analysis. The XRD patterns obtained for samples A4 ($Mg_{78}Zn_7Sr_{15}$) and A8 ($Mg_{35}Zn_{55}Sr_{10}$) are shown in Fig. 5. As can be seen in Fig. 5, a series of the same peaks with a little angle shift were observed in samples A4 and A8, which corresponds to $Mg_{15-x}Zn_xSr_3$. In Fig. 5(a), the phases $Mg_{17}Sr_2$ and $Mg_{15-x}Zn_xSr_3$ were indentified according to their characteristic peaks, which are in agreement with the observed results from the equilibrated sample A4 with metallographic method (see Fig. 4a). In Fig. 5(b), series of uncertain peaks were observed which shall belong to IM3.

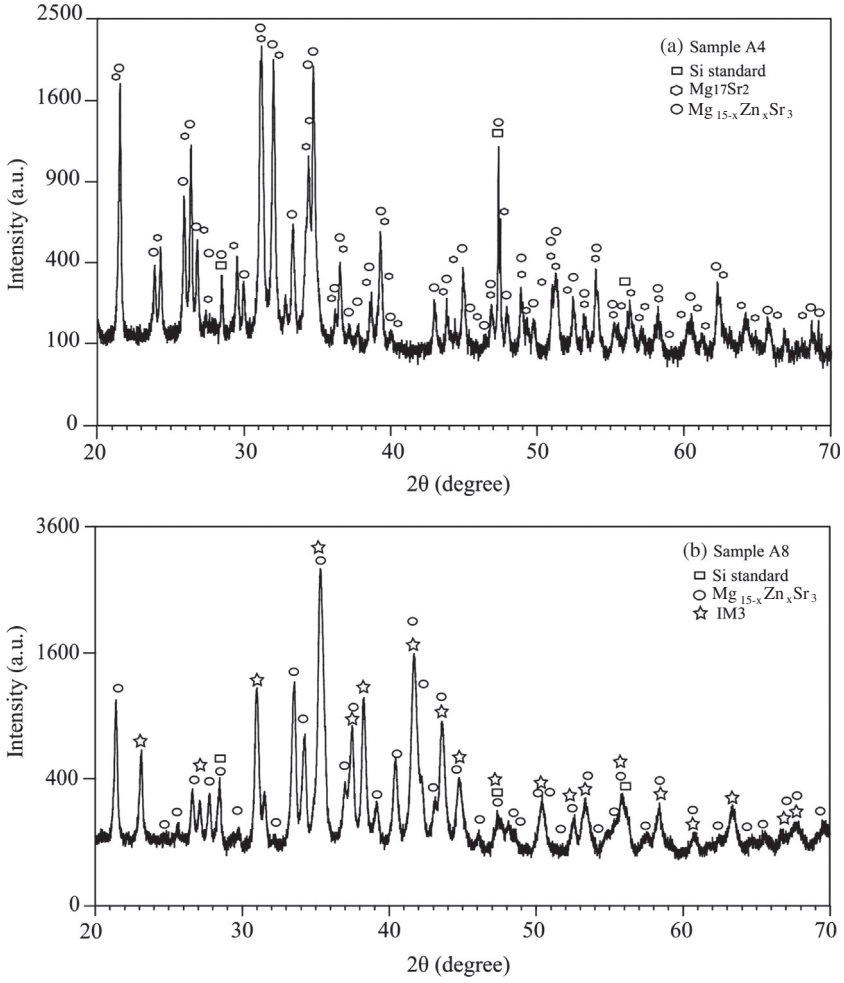

Fig. 5. XRD patterns obtained for samples: (a) A4 ($Mg_{78}Zn_7Sr_{15}$) and (b) A8 ($Mg_{35}Zn_{55}Sr_{10}$).

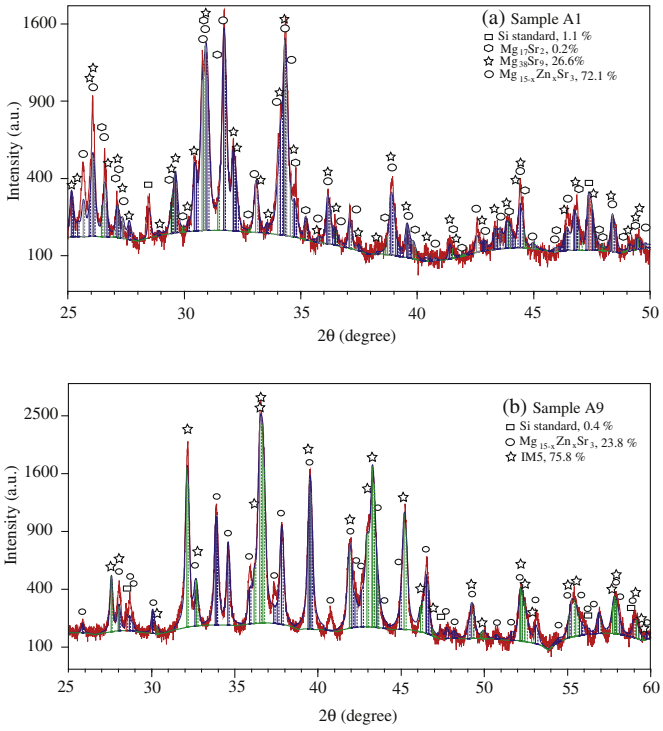

Fig. 6. XRD patterns refinement results of samples: (a) A1 ($Mg_{83}Zn_1Sr_{16}$) and (b) A9 ($Mg_{20}Zn_{65}Sr_{15}$).

Table 2
The chemical composition of the $Mg_{15-x}Zn_xSr_3$ compound as determined by EPMA and Rietveld analysis.

Sample no.	Composition determined (at.%)						Unit cell parameters (Å) obtained from Rietveld analysis	
	EPMA			Rietveld analysis				
	Mg	Zn	Sr	Mg	Zn	Sr	a	c
A1	81.6	1.3	17.1	82.0	1.4	16.7	10.455	10.839
A4	73.2	11.9	14.9	75.0	8.3	16.7	10.340	10.758
A5	69.0	14.7	16.3	70.6	12.7	16.7	10.243	10.655
A6	60.0	24.8	15.2	58.2	25.1	16.7	9.983	10.427
A7	39.6	44.3	16.1	40.4	42.9	16.7	9.688	10.179
A8	33.8	49.5	16.7	34.0	49.3	16.7	9.611	10.121
A9	24.9	58.8	16.3	25.5	57.8	16.7	9.520	10.015

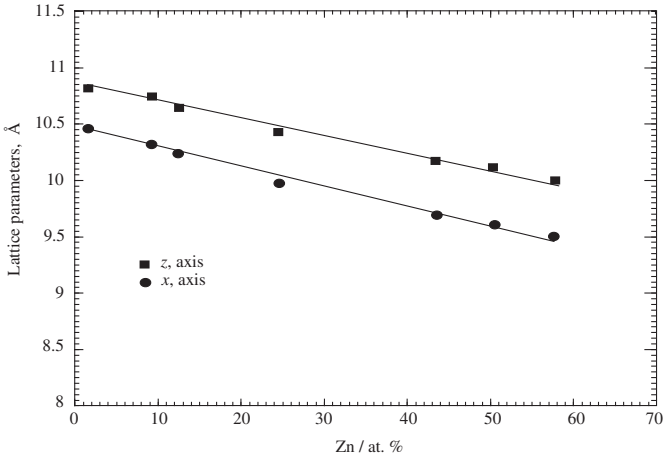

Fig. 8. Unit cell parameters versus Mg content.

All the compositions of the constituent phases of the equilibrated Mg–Zn–Sr ternary equilibrated samples are analyzed by EPMA and listed in Table 1. A nearly constant composition value of 16.7 in atomic percentage of Sr in the $Mg_{15-x}Zn_xSr_3$ compound was obtained in all key samples A1–A9 within the measurement error limits. The phase equilibrium relationships of $Mg_{15-x}Zn_xSr_3$ compound in the isothermal section of the Mg–Zn–Sr ternary system at 300 °C obtained in the present work are shown in Fig. 3.

Combining the measurement results of diffusion couple and equilibrated samples using EPMA and SEM/EDS techniques, the solid solubility limits of $Mg_{15-x}Zn_xSr_3$ were obtained in the present work. The formula of this compound is presented as $Mg_{15-x}Zn_xSr_3$ ($0.24 \le x \le 10.58$) at 300 °C.

3.2. Crystal structure analysis for $Mg_{15-x}Zn_xSr_3$

Full patterns refinement of samples A1 and A4–A9 has been carried out by the Rietveld method. Combining Pearson's crystallographic database [29] with the Rietveld analysis, the new $Mg_{15-x}Zn_xSr_3$ compound was found to crystallize in hexagonal $P6_3/mmc$ (194) space group and has the $Ni_{11}Si_4Sc_3$ prototype. This is the same structure type as $Mg_{11}Zn_4Ca_3$ (IM1) compound in the Mg–Zn–Ca ternary system reported by Zhang et al. [30,31]. The sites of 6h (1) ($x = 0.5618$, $y = 0.1236$, $z = 0.25$), 4f, 2b, and 12k are occupied with Mg and Zn atoms to form the continuous solid solubility, and the site of 6h (2) ($x = 0.192$, $y = 0.384$, $z = 0.25$) are occupied with Sr.

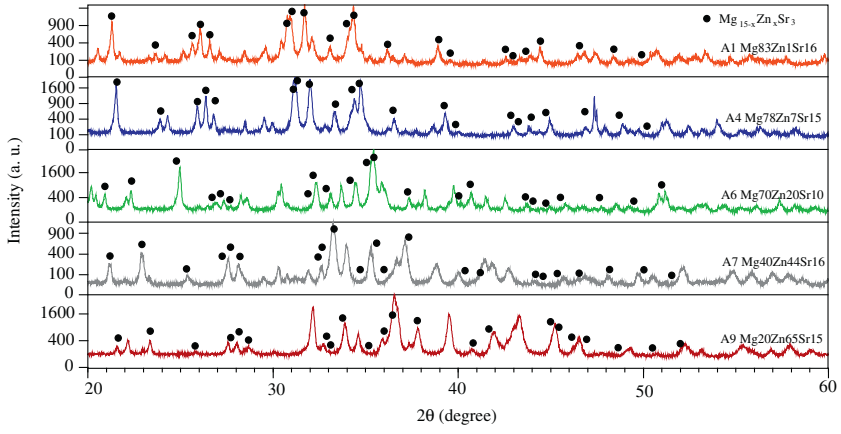

Fig. 7. XRD patterns of samples A1, A4, A6, A7 and A9 obtained by powder XRD diffraction.

Fig. 6(a) shows the XRD patterns refinement result of sample A1 ($Mg_{83}Zn_1Sr_{16}$) which contains three phases $Mg_{17}Sr_2 + Mg_{38}Sr_9 + Mg_{15-x}Zn_xSr_3$. It demonstrates the Rietveld analysis for the $Mg_{17}Sr_2$, $Mg_{38}Sr_9$, and $Mg_{15-x}Zn_xSr_3$ phases in sample A1, and the analyzed volume fractions of each phase with Rietveld analysis are in reasonable agreement with the results observed by SEM as shown in Fig. 4(c). Fig. 6(b) shows the Rietveld analysis results of sample A9 ($Mg_{20}Zn_{65}Sr_{15}$). The identified phase composition and the lattice parameters of the $Mg_{15-x}Zn_xSr_3$ compound obtained from seven samples by XRD Rietveld analysis and EPMA analysis are summarized in Table 2. The phase relations obtained from XRD after refinement analysis show great consistency with the results obtained by EPMA.

The XRD patterns of samples A1, A4, A6, A7 and A9 obtained by powder XRD diffraction are summarized in Fig. 7. According to the solid solubility measured by EPMA in the present work, the Mg and Zn substitute on another at a constant Sr composition in the $Mg_{15-x}Zn_xSr_3$ compound. The substitution of Mg by Zn, which has a smaller atomic radius, decreases the unit cell parameters. This is confirmed by the increase of 2θ values of the peak positions in the samples A1, A4, A6, A7 and A9 due to the increasing Zn concentration, as shown in Fig. 7. As shown in Figs. 5–7, the diffraction peaks from $Mg_{15-x}Zn_xSr_3$ crystals show a little broadening which may due to the small powder size obtained in grinding process. The broadening affection has been considered during our Rietveld analysis with certain parameters.

The variations of cell parameters with Mg concentration are shown in Fig. 8, where substitution of Mg by Zn decreases the unit cell parameters *a* and *c*, this is also shown in more details in Table 2. The linear relation between the lattice parameters and Mg clearly indicating the occurrence of substitutional solid solubility of Mg and Zn.

Table 3 shows the refined structural parameters of the $Mg_{15-x}Zn_xSr_3$ compound and the reliability factors. The fractional atomic occupancy of 6h, 6g, 4f, 2b, and 12k sites of $Mg_{15-x}Zn_xSr_3$ compound have been determined as a function of the Mg content, as shown in Fig. 9. The current experimental results obtained by Rietveld analysis of crystallographic and the site occupancy show similar results compared to the previous results reported for $Mg_{11}Zn_4Ca_3$ [30] compounds, which have the same crystal structure.

4. Conclusions

The solid solubility limits and crystal structure of the ternary compound $Mg_{15-x}Zn_xSr_3$ in the Mg–Zn–Sr system have been determined for the first time. The formula of this compound is suggested to be $Mg_{15-x}Zn_xSr_3$ ($0.24 \le x \le 10.58$) according its solid solubility limits at 300 °C. It has hexagonal $P6_3/mmc$ structure, 194 space group and $Ni_{11}Si_4Sc_3$ prototype.

The site occupancy of $Mg_{15-x}Zn_xSr_3$ was obtained using Rietveld analysis of XRD patterns. The site occupancies of 6h (1) ($a = 0.5618$,

Table 3
Refined crystal structure parameters of the $Mg_{15-x}Zn_xSr_3$ compound.

Sample no.	Wyckoff Position	*x*	*y*	*z*	Occupancy (%)			Reliability factors		
					Mg	Zn	Sr	R_e	R_{wp}	S
A1	12k	0.1641	0.3228	0.5827	98.5	1.5	0	9.64	16.41	2.89
	6h (1)	0.5618	0.1236	0.2500	100	0	0			
	6g	0.5000	0	0	93.3	6.7	0			
	4f	0.3333	0.6667	0.0086	100	0	0			
	2b	0	0	0.2500	100	0	0			
	6h (2)	0.1920	0.3840	0.2500	0	0	100			
A4	12k	0.1614	0.3228	0.5857	91.4	8.6	0	8.16	19.60	5.76
	6h (1)	0.5618	0.1236	0.2500	90.8	9.2	0			
	6g	0.5000	0	0	76.3	23.7	0			
	4f	0.3333	0.6667	0.0086	100	0	0			
	2b	0	0	0.2500	100	0	0			
	6h (2)	0.1920	0.3840	0.2500	0	0	100			
A5	12k	0.1614	0.3228	0.5857	89.9	11.1	0	12.95	25.17	3.77
	6h (1)	0.5618	0.1236	0.2500	80.5	19.5	0			
	6g	0.5000	0	0	62.7	37.3	0			
	4f	0.3333	0.6667	0.0086	100	0	0			
	2b	0	0	0.2500	100	0	0			
	6h (2)	0.1920	0.3840	0.2500	0	0	100			
A6	12k	0.1614	0.3228	0.5857	80.0	20.0	0	7.92	21.54	7.39
	6h (1)	0.5618	0.1236	0.2500	45.6	54.4	0			
	6g	0.5000	0	0	52.3	47.7	0			
	4f	0.3333	0.6667	0.0086	100	0	0			
	2b	0	0	0.2500	94.3	5.7	0			
	6h (2)	0.1920	0.3840	0.2500	0	0	100			
A7	12k	0.1614	0.3228	0.5857	77.4	22.6	18	12.71	30.19	5.64
	6h (1)	0.5618	0.1236	0.2500	22.7	77.3	0			
	6g	0.5000	0	0	5.4	94.6	0			
	4f	0.3333	0.6667	0.0086	74.0	26.0	0			
	2b	0	0	0.2500	30.3	69.7	0			
	6h (2)	0.1920	0.3840	0.2500	0	0	100			
A8	12k	0.1614	0.3228	0.5857	74.7	25.3	0	7.70	17.28	5.03
	6h (1)	0.5618	0.1236	0.2500	0	100	0			
	6g	0.5000	0	0	0	100	0			
	4f	0.3333	0.6667	0.0086	68.3	31.7	0			
	2b	0	0	0.2500	28.1	71.9	0			
	6h (2)	0.1920	0.3840	0.2500	0	0	100			
A9	12k	0.1614	0.3228	0.5857	63.0	37.0	0	7.83	15.06	3.70
	6h (1)	0.5618	0.1236	0.2500	0	100	0			
	6g	0.5000	0	0	0	100	0			
	4f	0.3333	0.6667	0.0086	31.3	68.7	0			
	2b	0	0	0.2500	17.5	72.5	0			
	6h (2)	0.1920	0.3840	0.2500	0	0	100			

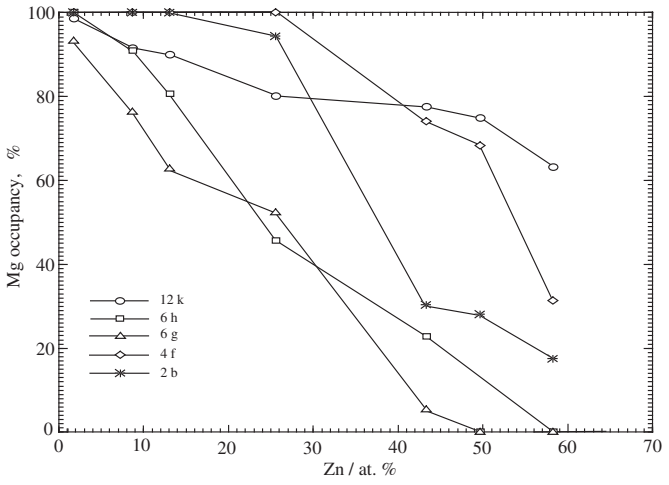

Fig. 9. The fractional atomic occupancy of 6h, 6g, 4f, 2b, and 12k sites variations with Mg content.

$b = 0.1236$, $c = 0.25$), 4f, 2b, and 12k have been presented as a function of Mg concentration.

Acknowledgments

Financial support from General Motors of Canada Ltd., and the Natural Sciences and Engineering Research Council of Canada through the CRD grant program is gratefully acknowledged. The support in the experimental part from Mr. Tian Wang, Mr. Xin Zhang, and Dr. Dmytro Kevorkov from Concordia University, and Dr. Shi Lang from McGill University is acknowledged by the authors.

References

[1] I. Polmear, Magnesium alloys and applications, Mater. Sci. Technol. Lond. 10 (1994) 1–16.
[2] Y. Sun, B. Zhang, Y. Wang, et al., Preparation and characterization of a new biomedical Mg–Zn–Ca alloy, Mater. Des. 34 (2012) 58–64.
[3] Q. Chen, D. Shu, Z. Zhao, et al., Microstructure development and tensile mechanical properties of Mg–Zn–RE–Zr magnesium alloy, Mater. Des. 40 (2012) 488–496.
[4] H. Li, W. Du, S. Li, et al., Effect of Zn/Er weight ratio on phase formation and mechanical properties of as-cast Mg–Zn–Er alloys, Mater. Des. 35 (2012) 259–265.
[5] K.U. Kainer, F. Kaiser, Magnesium Alloys and Technology, Wiley Online Library, 2003.
[6] M.M. Avedesian, H. Baker, ASM specialty handbook: magnesium and magnesium alloys, ASM Inter., 2741999.
[7] J. Chen, J. Wei, H. Yan, et al., Effects of cooling rate and pressure on microstructure and mechanical properties of sub-rapidly solidified Mg–Zn–Sn–Al–Ca alloy, Mater. Des. 45 (2013) 300–307.
[8] J. Wang, R. Liu, T. Luo, et al., A high strength and ductility Mg–Zn–Al–Cu–Mn magnesium alloy, Mater. Des. 47 (2013) 746–749.
[9] X. Chen, L. Liu, J. Liu, et al., Microstructure, electromagnetic shielding effectiveness and mechanical properties of Mg–Zn–Y–Zr alloys, Mater. Des. 65 (2015) 360–369.
[10] D. Wu, R.S. Chen, W.N. Tang, et al., Influence of texture and grain size on the room-temperature ductility and tensile behavior in a Mg–Gd–Zn alloy processed by rolling and forging, Mater. Des. 41 (2012) 306–313.
[11] W. Zhang, M. Li, Q. Chen, et al., Effects of Sr and Sn on microstructure and corrosion resistance of Mg–Zr–Ca magnesium alloy for biomedical applications, Mater. Des. 39 (2012) 379–383.
[12] M. Cong, Z. Li, J. Liu, et al., Effect of Sr on microstructure, tensile properties and wear behavior of as-cast Mg–6Zn–4Si alloy, Mater. Des. 53 (2014) 430–434.
[13] Y. Zhang, L. Yang, J. Dai, et al., Effect of Ca and Sr on the compressive creep behavior of Mg–4Al–RE based magnesium alloys, Mater. Des. 63 (2014) 439–445.
[14] E. Baril, P. Labelle, M. Pekguleryuz, Elevated temperature Mg–Al–Sr: creep resistance, mechanical properties, and microstructure, JOM J. Miner. Met. Mater. Soc. 55 (2003) 34–39.
[15] K. Hirai, H. Somekawa, Y. Takigawa, K. Higashi, Effects of Ca and Sr addition on mechanical properties of a cast AZ91 magnesium alloy at room and elevated temperature, Mater. Sci. Eng. A 403 (2005) 276–280.
[16] Y. Nakaura, A. Watanabe, K. Ohori, Effects of Ca, Sr additions on properties of Mg–Al based alloys, Mater. Trans. 47 (2006) 1031.
[17] H.S. Brar, J. Wong, M.V. Manuel, Investigation of the mechanical and degradation properties of Mg–Sr and Mg–Zn–Sr alloys for use as potential biodegradable implant materials, J. Mech. Behav. Biomed. 7 (2012) 87–95.
[18] H. Li, S. Pang, Y. Liu, et al., Biodegradable Mg–Zn–Ca–Sr bulk metallic glasses with enhanced corrosion performance for biomedical applications, Mater. Des. 67 (2015) 9–19.
[19] R. Agarwal, S.G. Fries, H.L. Lukas, G. Petzow, F. Sommer, T.G. Chart, G. Effenberg, Assessment of the magnesium–zinc system, Z. Metallkd. 83 (1992) 216–223.
[20] A. Nayeb-Hashemi, J. Clark, The Mg–Sr (magnesium–strontium) system, J. Phase Equilib. 7 (1986) 149–156.
[21] G. Bruzzone, F. Merlo, The Sr–Zn system, J. Less-Common Met. 92 (1983) 75–79.
[22] M. Aljarrah, U. Aghaulor, M. Medraj, Thermodynamic assessment of the Mg–Zn–Sr system, Intermetallics 15 (2007) 93–97.
[23] A.T. Dinsdale, SGTE data for pure elements, Calphad 15 (1991) 317–425.
[24] J. Wang, P. Hudon, D. Kevorkov, P. Chartrand, I.-H. Jung, M. Medraj, Experimental and thermodynamic study of the Mg–Sn–In–Zn quaternary system, J. Alloys Compd. 588 (2014) 75–95.
[25] J. Wang, N. Miao, P. Chartrand, I.-H. Jung, Thermodynamic evaluation and optimization of the (Na + X) binary systems (X = Ag, Ca, In, Sn, Zn) using combined Calphad and first-principles methods of calculation, J. Chem. Thermodyn. 66 (2013) 22–33.
[26] J. Wang, P. Hudon, D. Kevorkov, P. Chartrand, I.-H. Jung, M. Medraj, Thermodynamic and experimental study of the Mg–Sn–Ag–In quaternary system, J. Phase Equilib. Diffus. 35 (2014) 284–313.
[27] J. Wang, I.-H. Jung, P. Chartrand, Thermodynamic description of the Ag–(Ca, Li, Zn) and Ca–(In, Li) binary systems, Calphad 50 (2015) 68–81.
[28] J. Wang, Y.N. Zhang, I.-H. Jung, P. Chartrand, M. Medraj, Experimental study on the phase equilibria of Mg–Zn–Ag ternary system at 300 °C, J. Alloys Compd. 639 (2015) 593–601.
[29] P. Villars, K. Cenzual, Pearson's Crystal Data, Crystal Structure Database for Inorganic Compounds, ASM Inter, Materials Park (OH), 2007.
[30] Y.N. Zhang, D. Kevorkov, X.D. Liu, F. Bridier, P. Chartrand, M. Medraj, Homogeneity range and crystal structure of the $Ca_2Mg_5Zn_{13}$ compound, J. Alloys Compd. 523 (2012) 75–82.
[31] Y.N. Zhang, D. Kevorkov, J. Li, E. Essadiqi, M. Medraj, Determination of the solubility range and crystal structure of the Mg-rich ternary compound in the Ca–Mg–Zn system, Intermetallics 18 (2010) 2404–2411.